PERGAMON

Atmospheric Environment 33 (1999) 3119–3132

ATMOSPHERIC ENVIRONMENT

A numerical model for the simulation of SO_2 concentrations in the Kyongin region, Korea

Soon-Ung Park*, Cheol-Hee Kim

Department of Atmospheric Sciences, Seoul National University, San 56-1 Shilim-Dong Kwanak-Ku, Seoul, 151-742, South Korea

Received 16 September 1997; accepted 18 August 1998

Abstract

A method for solving the non-reactive tracer continuity equation using a time splitting technique and a Galerkin technique with chapeau functions as finite elements for the horizontal advection has been developed and employed to simulate SO_2 concentrations in the Kyongin region in Korea for a synoptic case of high pollution potential days in autumn with the relatively strong southwesterly geostrophic wind at the 850 hPa pressure level. The paired comparisons between hourly observed and the simulated SO_2 concentrations are made to test the model performance. The result indicates that the present model simulates quite well horizontal distribution patterns of SO_2 concentration. However, the simulated concentrations depend largely on the emission rate, suggesting the importance of accurate source identification for the accurate simulation of the concentration field.

Keywords: SO_2 concentration simulation; Advection–diffusion scheme; Diagnostic wind field; Galerkin technique

1. Introduction

Recent air quality in South Korea indicates that annual mean SO_2, TSP and NO_2 concentrations exceed the national ambient air quality standards in the Seoul Metropolitan area and most big cities in South Korea for high air pollution potential days. This leads us to consider some measures for the improvement of air quality in Korea.

Air quality models are a key component in determining pollution control requirements. To ensure that the best techniques are used for estimating pollutant concentrations for assessing control strategies and for specifying emission limits (Touma et al., 1995).

However, the quality of the air quality simulation models is restricted by the meteorological fields and the numerical methodology to evaluate diffusion advection processes in the atmosphere. Most air quality simulation models employ simple diagnostic wind fields that are obtained by extrapolation and/or interpolation of sparse observational data. Often these fields are adjusted to satisfy constraints derived from the mass conservation (Sherman, 1978; Davis et al., 1984). Gaussian concentration distributions (Pielke, 1984), first-order closure techniques (Davis et al., 1984), or stochastic techniques (Lange, 1978) are then used to represent turbulent diffusion of a contaminant in the diagnosed meteorological fields. The advantages of these models are their simplicity, general applicability in simple atmospheric conditions, and most important, their limited computational demands. Of course, models that employ these methods have serious limitations including their inability

*Corresponding author. Fax: 82 2 880 6715; e-mail: supark@snupbl.snu.ac.kr.

1352-2310/99/$ – see front matter
PII: S1352-2310(98)00335-5

to simulate complex dynamic features not explicitly measured.

Some case studies have been done to overcome these limitations using the mesoscale three-dimensional modeling system with four-dimensional data assimilation procedure such as the regional atmospheric modeling system (RAMS) developed at Colorado State University (Pielke et al., 1992). However, the results indicate that the mesoscale model has the potential for improving the prognostic capabilities of atmospheric modeling for local contaminant transport but still is on the experimental stage (Fast et al., 1995).

Recently Park (1992) has developed a three-dimensional meteorological fields based on a similarity theory in the surface layer and a Rossby number similarity theory in the boundary layer using surface meteorological observation data and successfully used for the air quality simulation (Park, 1994).

To get the pollutant concentration in an Eulerian frame work, we need to solve the three-dimensional tracer continuity equation numerically. This requires a proper numerical scheme which can handle the advection and diffusion processes properly. One of the powerful numerical methods to solve the advection–diffusion equation is to use the time split model that replaces the three-dimensional equation with three equivalent one-dimensional equations so that the numerical analogs of the one-dimensional equations are much simpler than the numerical analogs for the three-dimensional equations (Carmichael et al., 1986; Toon et al., 1988).

The purpose of this study is to develop an advanced atmospheric transport and diffusion modeling system in the terrain following coordinates using a time splitting technique and a Galerkin technique with chapeau functions as finite elements for the horizontal advection and to simulate the SO_2 concentration in the Kyongin region in Korea, based upon a diagnosed three-dimensional meteorological field using routinely available surface observation data for the case of the high air pollution potential days and to test the sensitivity of the model for the emission rate.

2. The tracer continuity equation in the terrain following coordinates

The flux form of the continuity equation for the tracer concentration C, at time t, being advected by the wind u, v and w^* in the terrain following coordinates, mixed by diffusion coefficients K_H in horizontally and K_z vertically in an atmosphere with coordinates x, y, z^* is given by (e.g., Toon et al., 1988)

$$\frac{\partial C}{\partial t}+\frac{\partial}{\partial x}(uC)+\frac{\partial}{\partial y}(vC)+\frac{\bar{s}}{\bar{s}-z_g}\frac{\partial}{\partial z^*}(w^*C)$$
$$-\frac{\partial}{\partial x}\left(K_H\frac{\partial C}{\partial x}\right)+\frac{\partial}{\partial y}\left(K_H\frac{\partial C}{\partial y}\right)$$
$$-\left(-\frac{\bar{s}}{\bar{s}-z_g}\right)^2\frac{\partial}{\partial z^*}\left(K_z\frac{\partial C}{\partial z^*}\right)$$
$$=(P-L)\left(\frac{\bar{s}-z_g}{\bar{s}}\right), \tag{1}$$

where P is the production rate and L the loss rate. We choose the terrain following coordinate in which the vertical coordinate z^* is given by

$$z^*=\bar{s}\frac{z-z_g(x,y)}{\bar{s}-z_g(x,y)}, \tag{2}$$

where $\bar{s}$ is the height of the model top which is assumed to be constant, $z_g(x, y)$ the height of the topography, and z is the height in cartesian coordinates.

The vertical velocity w^*, in the terrain following coordinates is given by

$$w^*=\frac{z^*-\bar{s}}{\bar{s}-z_g}\left(u\frac{\partial z_g}{\partial x}+v\frac{\partial z_g}{\partial y}\right)+\frac{\bar{s}}{\bar{s}-z_g}w \tag{3}$$

and the continuity equation is

$$\frac{\partial u}{\partial x}+\frac{\partial v}{\partial y}+\frac{\partial w^*}{\partial z^*}+\frac{1}{\bar{s}-z_g}\left(u\frac{\partial z_g}{\partial x}+v\frac{\partial z_g}{\partial y}\right)=0. \tag{4}$$

2.1. Time splitting

The three-dimensional tracer continuity equation in Eq. (1) can be solved numerically by replacing it with three equivalent one-dimensional equations by using the time splitting method. The advantage of this replacement is that the numerical analogs of the one-dimensional equations are much simpler than the numerical analogs for the three-dimensional equations (Carmichael et al., 1986).

We replace Eq. (1) with

$$\frac{\partial C}{\partial t}+\frac{\partial}{\partial x}(uC)-\frac{\partial}{\partial x}\left(K_H\frac{\partial C}{\partial x}\right)=0, \tag{5a}$$

$$\frac{\partial C}{\partial t}+\frac{\partial}{\partial y}(vC)-\frac{\partial}{\partial y}\left(K_H\frac{\partial C}{\partial y}\right)=0, \tag{5b}$$

$$\frac{\partial C}{\partial t}+\frac{\bar{s}}{\bar{s}-z_g}\frac{\partial}{\partial z^*}(w^*C)-\left(\frac{\bar{s}}{\bar{s}-z_g}\right)^2\frac{\partial}{\partial z^*}\left(K_z\frac{\partial C}{\partial z^*}\right)$$
$$=(P-L)\left(\frac{\bar{s}-z_g}{\bar{s}}\right). \tag{5c}$$

These equations are solved sequentially (5a), (5b), (5c) and then (5c), (5b), (5a) to complete two time steps. Reversing the order of the solution after each time step provides slightly greater accuracy. After Eq. (5a) is solved over the time step, the new concentration is used to solve Eq. (5b) and so forth.

2.2. Numerical analogs for horizontal advection and vertical transport

The numerical simulation of Eqs. (5a) and (5b) are solved with a Galerkin technique (Haltiner and Williams, 1980) with chapeau functions as finite elements, and a Crank–Nicolson time step (Chock and Dunker, 1983; Pepper et al., 1979; Carmichael et al., 1980, 1986). The advantages for this technique are that the tracer concentrations need to be retained only at one time step so memory requirements are minimized.

The one-dimensional discretized equations can be put into tridiagonal form which is computationally stable and very fast. The transport coefficients are independent of concentration so that multiple species can be transported using the same set of coefficients, which again saves computer time. Irregular grid spacing can be accommodated. The code is semi-implicit so it is unconditionally stable. The numerics are quite accurate even when sharp gradients are present and exactly conserve mass. The numerical solutions for Eqs. (5a) and (5b) are obtained with the expansion of the variables of interest using a set of tent-shaped piecewise linear functions, the so-called chapeau functions that extend over a single neighboring grid point as shown in Fig. 9.

Following this expansion we employ the Galerkin technique (Haltiner and Williams, 1980) and integrate the product of the error in solving Eq. (5) with the basis functions over the domain and then set this integral to zero. The Galerkin procedure is illustrated in Appendix A.1. Next we approximate the time derivatives using the Crank–Nicolson scheme. The finite forms of Eqs. (5a), (5b) and (5c) are given in Appendix A.2.

2.3. Boundary conditions for horizontal advection

With a spatially limited domain it is useful to have boundary conditions that may be controlled. The normal method of handling the transport at the grid boundary is to truncate the last chapeau function as illustrated in Fig. 9.

The boundary flux is estimated by expanding the Galerkin integral of the advection term by parts. The results are given in Appendix A.3.

The majority of numerical algorithms as well as the chapeau algorithm for advection produce computational noise which results in negative concentrations in the vicinity of strong concentration gradients. Mahlman and Sinclair (1977) scheme that conserves mass and computationally very simple has been used in this study to eliminate negative number.

2.4. Parameterizations of eddy exchange coefficients

The horizontal eddy exchange coefficient K_H based on Mahrer and Pielke (1977) is estimated as

$$K_H = 0.36(\Delta x \Delta y)\left[\left(\frac{du}{dx}\right)^2 + \left(\frac{dv}{dy}\right)^2\right]^{1/2}, \quad (6)$$

where Δx and Δy are the grid distance in the x and y directions, respectively. While the vertical eddy diffusivity is given in Appendix B.

3. Air quality simulation over Kyongin region for the high pollution potential days in autumn

3.1. The meteorological model

The objective analysis methodology is used to provide a fast, objective, three-dimensional wind analyses in complex terrain by incorporating two important physical constraints of mass conservation and limitation of atmospheric stability on vertical displacement (Park, 1992). This method has been applied for the case of the high pollution potential days in autumn that has been identified by the complex potential index (Jung et al., 1996). The chosen synoptic case consists of 4 days in autumn seasons (26, 27 November 1991 and 18, 24 November 1992). The common synoptic feature of the chosen high pollution potential days is a broad area of high pressure at 850 hPa off the southwest coast of Japan leading to large-scale southerly winds over Korea and a weak zonal westerly winds at 500 hPa.

The three-dimensional diagnostic wind model has been used to construct diurnal varying wind and turbulent fields using the hourly averaged surface observation data obtained from sites indicated in Fig. 1 for the chosen synoptic case. The mass conserving three-dimensional wind fields in the 3 km × 3 km horizontal grid spacing with 15 vertical levels (2.5, 10, 20, 50, 100, 250, 500, 750, 1000, 1250, 1500, 1750, 2000, 3000 and 5000 m) are used to simulate the air quality in the Kyongin region of Korea (Fig. 1).

3.2. Emission data

The 2 km × 2 km gridded SO_2 emission estimates conducted by the National Institute of Environmental Research (1994) for the reference year of 1992 over the Seoul metropolitan area in the domain of 60 km × 60 km are used for the simulation of the air quality in the Kyongin region.

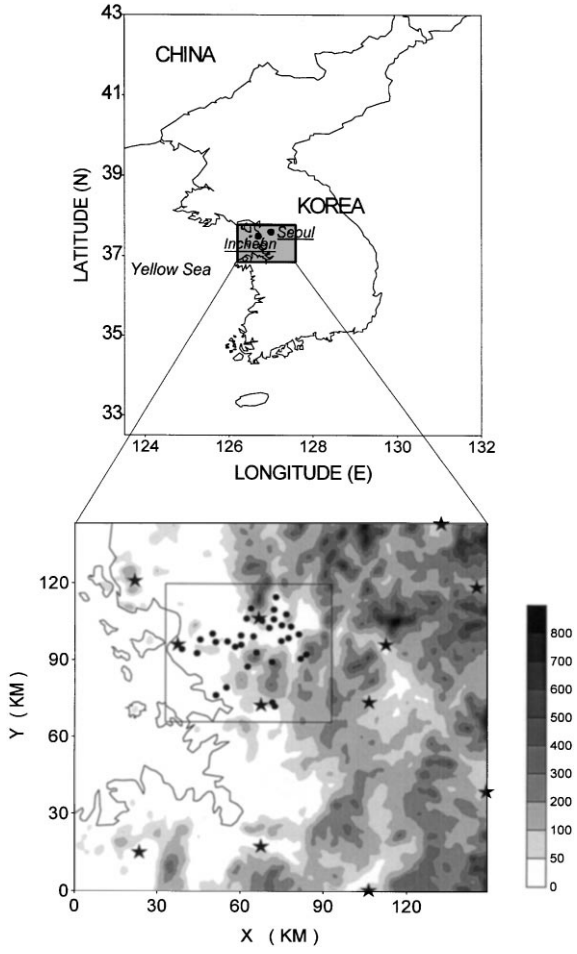

Fig. 1. The location of the analysis domain with the indication of the Kyongin region (the inner rectangle area in the bottom figure). Locations of meteorological observation stations (★) and air monitoring sites (●) are shown in the bottom figure.

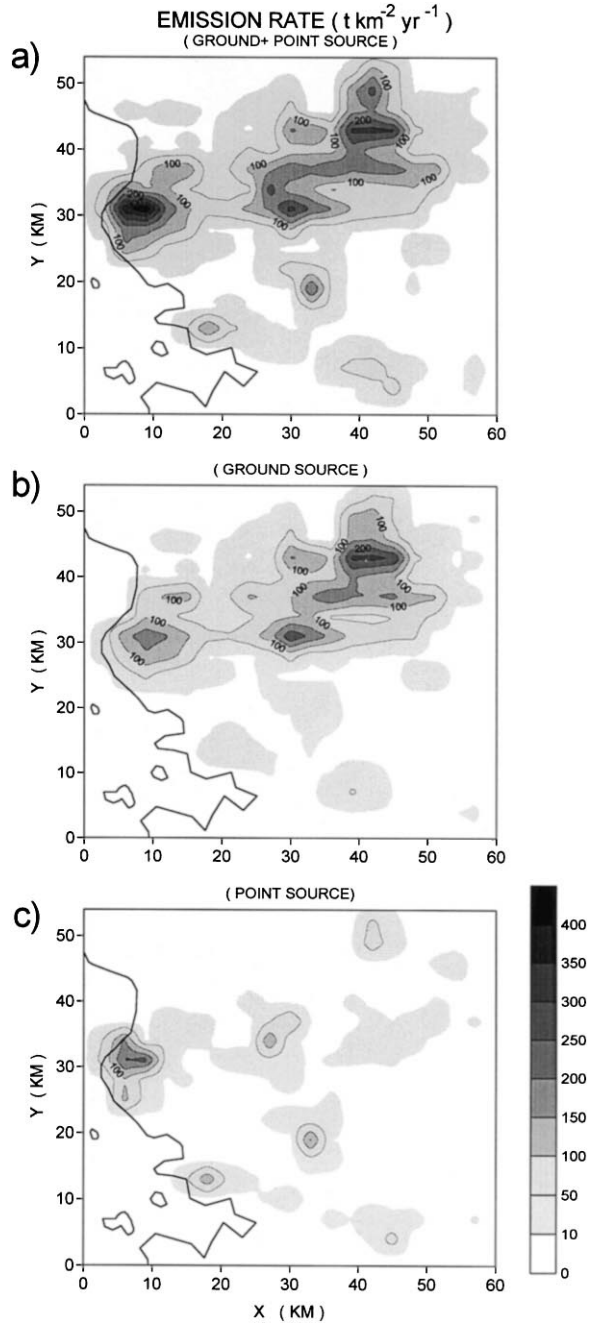

Fig. 2. Horizontal distributions of annual (a) total amount of SO_2 emissions ($t\,km^{-2}\,yr^{-1}$), (b) area source emissions ($t\,km^{-2}\,yr^{-1}$) and (c) point source emissions ($t\,km^{-2}\,yr^{-1}$).

Fig. 2 shows the horizontal distribution of the annual total amount of SO_2 emission (Fig. 2a) including area sources (Fig. 2b) and point sources (Fig. 2c) in the analysis domain. The main SO_2 source regions are big cities and some of them exceed the total emission rate of $200\,t\,km^{-2}\,yr^{-1}$.

The maximum ground emission is more than $260\,t\,km^{-2}\,yr^{-1}$. While the emissions from the point sources have their maximum value of $208\,t\,km^{-2}\,yr^{-1}$ at Incheon.

3.3. Initial conditions for the simulation of ground-level SO_2 concentrations

Presently developed algorithm has been applied for the chosen high pollution potential days with the emission data in Section 3.2. Initially the SO_2 concentration is assumed to be zero in the whole model domain and the emitted SO_2 pollutants from the area sources are assumed to be mixed in the lower 10 m layer immediately while the pollutants emitted from the elevated sources are mixed immediately in the layer where the sources are located.

Due to the lack of information on the stack heights we have assumed that all the stack heights of the point sources are 50 m. Therefore SO_2 emissions from the point sources are well mixed in the layer between 50 and 100 m above the ground.

The model simulation has been performed for the 48 h with the diurnal varying diagnosed meteorological field for the chosen synoptic condition. The results of the 48 h simulation are used as initial conditions for the next 24 h simulation of the ground-level SO_2 concentrations. The model has been spun up within 24 h. Therefore, the 48 h simulation time is long enough to get more reasonable initial distribution of SO_2 concentrations.

4. Results

4.1. Wind fields

Fig. 3 shows the simulated wind vectors to every other grid point 10 m above the ground at 0900, 1500, and 2100 LST for the high pollution potential days in autumn for the case of strong southwesterly geostrophic wind (6.7 m s^{-1} from 250° direction) at 850 hPa.

These simulated wind vectors are quite similar to the observed ones (not shown). The easterly winds along the coastline which are associated with the land breeze at 0900 LST (Fig. 3a) are veering with time due to the development of daytime sea breezes from the Yellow Sea and become completely westerly winds by 1100 LST. At 1500 LST (Fig. 3b), the westerly winds along the coastline are intensified while weak southwesterly flows keep to remain continuously in the eastern part of the analysis domain where rugged terrain is located. At 2100 LST (Fig. 3c) wind direction turnings from westerly winds to northwesterly occur along the coastline with strengthened intensities. The intensified westerly wind speed over the inland is also noticed.

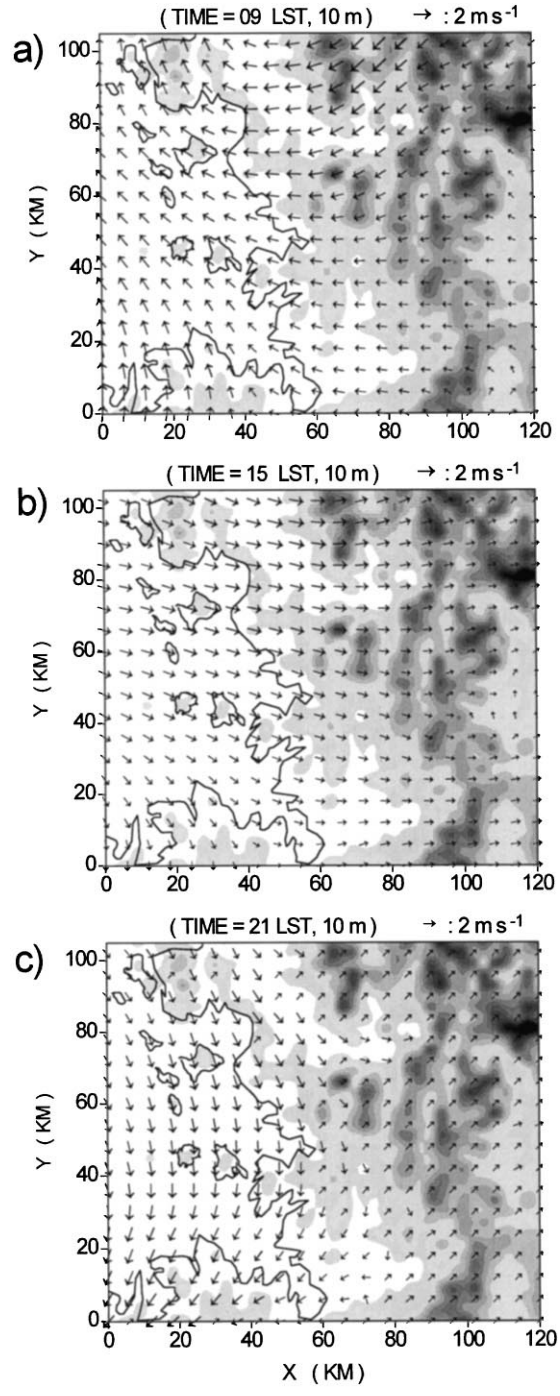

Fig. 3. Model simulated wind vectors at 10 m above the ground at (a) 0900, (b) 1500, and (c) 2100 LST.

4.2. Horizontal distribution of observed SO_2 concentrations

In order to minimize the impact of the large-scale meteorological conditions, hourly averaged concentrations for four days in two autumns belonging to the same synoptic condition of strong southwesterly geostrophic wind (6.7 m s^{-1} from 250° direction at 850 hPa) are selected. These selected days are also belonging to the high air pollution potential days.

Fig. 4a shows time variations of the horizontal distributions of the objectively analyzed observed hourly SO_2 concentrations using the data obtained from 32 monitoring sites in the analysis domain (Fig. 1). In the early morning hours the ground-level SO_2 concentrations follow the pattern of the ground source emissions (Fig. 2) with slightly shifted maxima to the south east of the maximum emissions due to the prevailing northerly flow in the lower layer. However, in the afternoon the maximum ground-level SO_2 concentration occurs inland

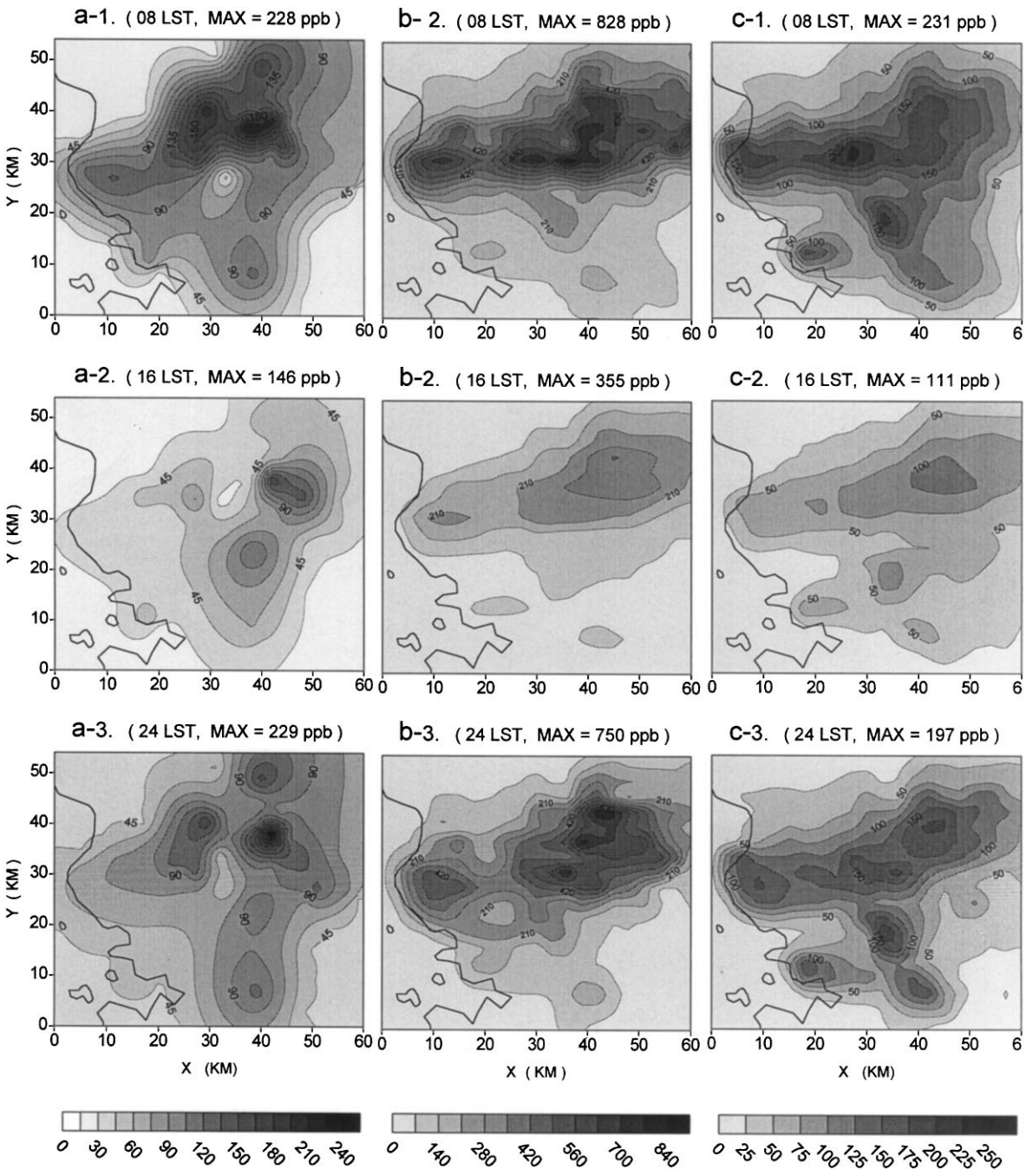

Fig. 4. Horizontal distributions of SO_2 concentrations (ppb) for the (a) objectively analyzed observation, (b) model simulation without emission reduction and (c) model simulation with the emission reduction.

regions with much reduced concentrations due to the intensifying sea breeze during the day. As the nighttime progresses the maximum ground level concentration zone extends westward where the large emission source exists.

4.3. Horizontal distribution of simulated SO_2 concentrations

Fig. 4b shows horizontal distributions of simulated ground-level SO_2 concentrations contributed by both

the area sources and point sources given in Fig. 2. In this simulation all the stack heights of the point sources are assumed to be 50 m. Simulation results (Fig. 4b) follow the pattern of emissions with maximum concentrations in the Incheon and Seoul area. However, there are large discrepancies in maximum concentrations between simulations and observations (Fig. 4a). The simulated maximum concentrations are 3–5 times greater than those of observations with greater values during the night.

Generally the discrepancies between simulations and observations stem from errors in the input data, such as emission inventories and meteorological data, as well as model's treatment of the physical processes and also improper characterization of point and area sources as indicated by Rao et al. (1985). To test model performance, we have run the model with the reduced emission by a factor of 2.5 in Incheon and Seoul where a large amount of emissions are contributed by residential heatings. The horizontal distribution of the reduced annual total amount of SO_2 emissions is shown in Fig. 5. The simulated results (Fig. 4c) indicate that the horizontal distribution pattern is more similar to the observed distribution of concentration than the result obtained by using the original source inventory data. The maximum concentration is reduced to factors of 3.2–4.4 of the non-reducted case with large decreases during the night.

Comparisons of the horizontal distribution of concentrations between the simulated result with the reduced emission rate (Fig. 4c) and the observations (Fig. 4a) show that the numerical model calculations show a slight bias toward underprediction during the daytime while a slightly overprediction during the night.

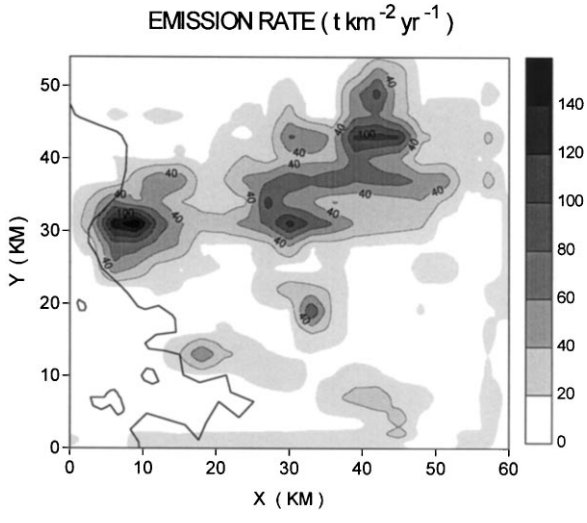

Fig. 5. Horizontal distributions of total annual amount of SO_2 emissions ($t\,km^{-2}\,yr^{-1}$) reduced by the factor of 2.5 in the Incheon and Seoul region.

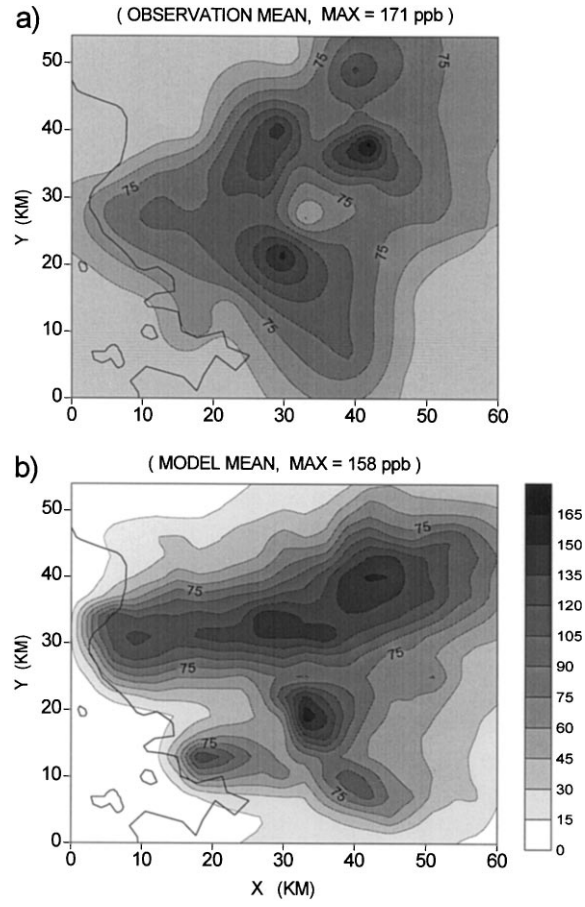

Fig. 6. Horizontal distributions of 24 hr averaged SO_2 concentrations of (a) observation and (b) model simulation with emission reduction.

Fig. 6 shows comparison of the horizontal distributions of 24 h-averaged SO_2 concentrations of observation and model simulation with the reduced emission. The distribution patterns are rather similar to each other except in the north eastern part of the analysis domain where air pollution monitoring sites are absent and in Incheon where the emission rate is relatively large. The simulated maximum concentration (158 ppb) is slightly lower than that of observation (171 ppb) in the analysis domain.

4.4. Area-averaged SO_2 concentrations

For our convenience, we subdivide the model domain into four regions as shown in Fig. 7 to examine the area-averaged concentration variations with time and for paired statistical analysis. Region 1 includes most of the

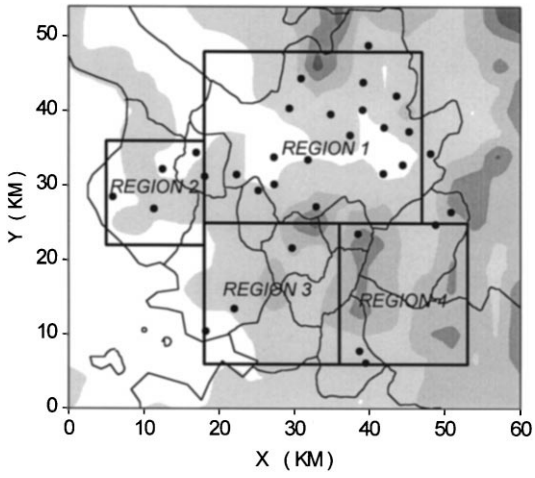

Fig. 7. Subdivision of the model domain into four regions for the statistical analysis and area mean concentration.

Seoul city area where scattered large emission sources are located. Region 2 includes Incheon city where large point sources are located. Regions 3 and 4 are, respectively, corresponding to the southwest and southeast suburban regions of Seoul.

Figs. 8a and b shows comparisons of the simulated and observed area averaged hourly SO_2 concentrations as functions of time of the day at four regions (Fig. 7) using the original emission inventory data and the reduced emission rate by a factor of 2.5, respectively.

Although the numerical model results simulate the same diurnal trend of observed concentrations including the morning and night peaks and the afternoon minimum, the magnitude of variation simulated by the model with the original emission data is about 3.3 times larger than the observed one in Regions 1 and 2, where emissions are large. However, the discrepancies are much reduced in Regions 3 and 4. The simulated daily mean value in Region 3 is higher by a factor of 1.5 while in Region 4 it is within a factor of 1.1 (Fig. 8a).

Much better simulations are seen in Fig. 8b for the case of the emission reduction by a factor of 2.5. The simulated area-average concentrations are in resonable agreement with the observed concentrations in all regions. However, more larger errors occur in the morning hours with a tendency toward overprediction.

4.5. Statistics of model performance evaluation

Statistical analysis of the simulations and the observations is performed using the methods discussed by Fox (1981). The objectively analyzed hourly observed SO_2 concentrations and the hourly simulated SO_2 concentrations in the 1 km × 1 km gridded domain are used for the statistical analysis.

The results of paired comparisons for the hourly SO_2 concentrations for the cases without and with emission reduction in Incheon and Seoul are, respectively, summarized in Tables 1 and 2.

The mean differences in Regions 1 and 2 are, respectively, 292.6 and 216.9 ppb for the case without emission reduction while they are 12.8 and 19.5 ppb with emission reduction, with a trend toward overprediction. However, those in Regions 3 and 4 are, respectively, 49.6 and 27.6 ppb without the emission reduction and 5.2 and 3.0 ppb with emission reduction. The index of agreement suggests that the simulations with the emission reduction are more accurate than those without the emission reduction in all chosen regions. The correlation coefficients for both cases (with and without emission reductions) are almost the same except in Regions 2 and 3 where slightly larger correlation coefficient occurs for the case of the emission reduction than the case without the emission reduction.

The root-mean-squared errors for the case of simulation without the emission reduction are 7.5, 5.6, 2.1 and 1.9 times higher than those of simulations with the emission reduction in the Regions 1, 2, 3 and 4, respectively. This clearly indicates that the emission reduction case gives much better simulation than the case of the non-reduction case. It also indicates that the emission reduction by a factor of 2.5 leads to rather large amount of the concentration reduction by a factor of 7.5. For the case of the emission reduction, unsystematic errors are larger than systematic errors in all regions but much larger unsystematic errors occur in Regions 3 and 4. This suggests that further refinement in the model is possible in Regions 1 and 2 to minimize the errors. The sources for systematic error may be improper emissions, meteorological data and the observed data. The fractional errors that are convenient for comparing model performance (Touma et al., 1995) are respectively, -0.13, -0.16, 0.03, and -0.01 in Regions 1, 2, 3 and 4 so that model predictions are within a factor of 1.3 of the measured values in all regions.

The correct characterization of the source as a point source or an area source is also important for the proper simulation of the concentration field. We have used the annual emission inventory data so that seasonal and diurnal variations can not be taken care of to simulate the SO_2 concentration. This may contribute to large discrepancies between simulated and observed concentrations.

5. Summary and conclusions

The numerical algorithms which we use to simulate the advection and diffusion in the terrain following

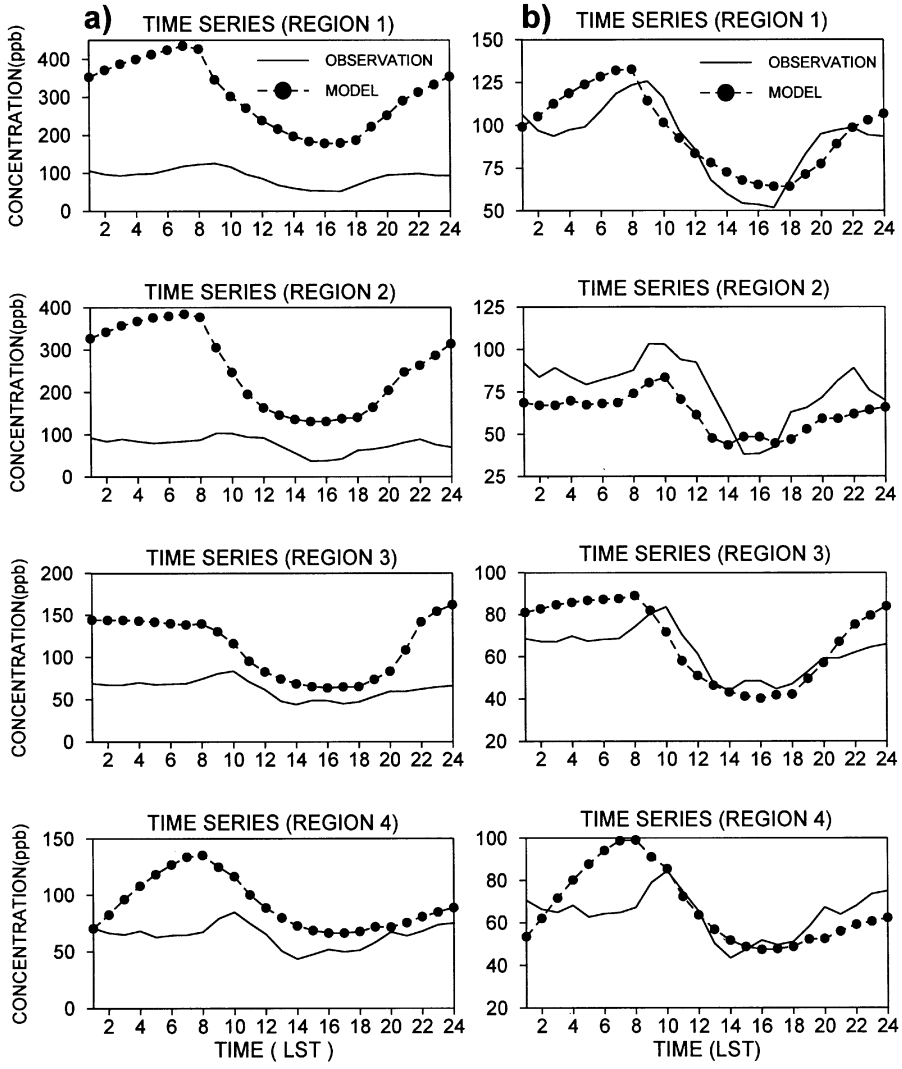

Fig. 8. Diurnal variations of the simulated (– –●– –) and observed (———) SO_2 concentrations averaged over each region for the cases of (a) without and (b) with emission reduction.

coordinate are described. The algorithms are used to simulate the SO_2 concentrations in Kyongin region of Korea for the high air pollution potential days in autumn. The diagnostically constructed three-dimensional meteorological fields described by Park (1992) and the emission inventory data conducted by the National Institute of Environmental Research (NIER, 1994) in the 2 km × 2 km gridded domain are used for the simulation. The environmental monitoring SO_2 concentration data in the analysis domain for the chosen days are obtained from the Ministry of Environment. These data are used for the model performance test. Statistical techniques chosen to determine the accuracy and uncertainty associated with the simulation model results include paired analysis.

A systematic comparison between the simulated and observed concentrations indicates that the inventorized emission rate is overestimated by a factor of 2.5 in Seoul and Incheon areas. This might be associated with the seasonal variation of emission rate mainly due to space heatings. The simulation results with the reduced emission rate by a factor of 2.5 reveal to be in reasonable agreement with the observed concentrations although there is a tendency toward overprediction in the morning hours. Statistical results based on paired comparisons clearly indicate that the emission rate is one of the most important parameters in the model input for the accurate simulation of the concentration field, but the horizontal distribution pattern is not affected by the emission rate change.

Table 1
Summary of paired comparisons for hourly SO_2 concentrations in various regions without emission reduction

	Region 1		Region 2		Region 3		Region 4	
	Obs. (O)	Model (S)	Obs. (O)	Model (S)	Obs. (O)	Model (S)	Obs. (O)	Model (S)
Sample size	6840		2112		6912		6912	
Range (ppb)	25.2–250.5	69.3–980.3	22.5–158.2	55.3–689.4	20.5–107.1	25.2–323.0	19.5–128.2	15.0–247.1
Mean (ppb)	104.0	396.6	80.3	297.2	62.0	111.6	63.7	91.3
Standard deviation (ppb)	38.5	168.4	26.6	142.7	15.4	57.9	20.7	39.2
Correlation coefficient	0.43		0.45		0.44		0.64	
Standard deviation of (S/O)	1.71		1.81		0.81		0.55	
Mean of (S/O)	4.11		3.84		1.80		1.48	
Mean of difference (S–O)	292.6		216.9		49.6		27.6	
Standard deviation of difference (ppb)	155.8		133.0		52.9		30.4	
Average absolute gross error (ppb)	292.7		216.9		51.5		30.5	
Root-mean-squared error for the difference (ppb)	331.5		254.4		72.5		41.1	
Index of agreement	0.38		0.33		0.41		0.71	
Mean fractional error	− 1.12		− 1.06		− 0.47		0.32	
Unsystematic MSE (UMSE)	23 122.9		16 289.2		2692.3		905.7	
Systematic MSE (SMSE)	85 756.1		48 421.4		2570.0		782.3	
UMSE/MSE (%)	21		26		51		53.7	
SMSE/MSE (%)	79		74		49		46.3	

Present study mainly pertains to develop numerical algorithms for the diffusion and advection of non-reactive air pollutants. These schemes could be used for the reactive pollutants provided that chemical reactions of pollutants in the gridded volume are included.

Acknowledgements

This research was partially supported by the Korea Science and Engineering Foundation under the grant No. 941-0400-018-2, and by the Ministry of Education in 1997 under the grant BSRI-97-5412.

Appendix A

A.1. The Galerkin procedure

The Galerkin procedure represents the dependent variables with a sum of functions that have a prescribed spatial structure to transform a partial differential equation into a set of ordinary differential equations for the coefficients that are normally a function of time. The most useful Galerkin methods are the spectral method and the finite element method. The spectral method, which employs orthogonal functions, while the finite element method employs functions that are zero except in a limited region where they are low-order polynomials.

The time splitted Eq. (5) is expressed in a general form

$$L(u) = f(x), \tag{7}$$

where L is a differential operator, u is the dependent variable and $f(x)$ is a specified forcing function. Suppose that Eq. (7) is to be solved in a domain $a \leqslant x \leqslant b$ and that appropriate boundary conditions are provided. Consider a series of linearly independent functions $\phi_i(x)$ that will be called basic functions. The next step is to approximate $u(x)$ with a finite series as

Table 2
Summary of paired comparisons for hourly SO_2 concentrations with the emission reduction by a factor of 2.5 in Incheon and Seoul

	Region 1		Region 2		Region 3		Region 4	
	Obs. (O)	Model (S)	Obs. (O)	Model (S)	Obs. (O)	Model (S)	Obs. (O)	Model (S)
Sample size	6840		2112		6912		6912	
Range (ppb)	25.2–250.5	32.8–231.2	22.5–158.2	18.4–186.0	20.5–107.1	7.5–217.4	19.5–128.2	6.8–164.3
Mean (ppb)	104.0	116.8	80.3	99.8	62.0	67.2	63.7	66.7
Standard deviation (ppb)	38.5	39.8	26.6	42.9	15.4	36.8	20.7	29.0
Correlation coefficient	0.42		0.36		0.37		0.66	
Standard deviation of (S/O)	0.49		0.65		0.54		0.42	
Mean of (S/O)	1.24		1.33		1.09		1.08	
Mean of difference (S–O)	12.8		19.5		5.2		3.0	
Standard deviation of difference (ppb)	42.0		41.5		34.2		21.7	
Average absolute gross error (ppb)	35.9		35.9		24.9		17.2	
Root-mean-squared error for the difference (ppb)	43.9		45.8		34.6		22.0	
Index of agreement	0.66		0.59		0.48		0.79	
Mean fractional error	− 0.13		− 0.16		0.03		− 0.01	
Unsystematic MSE (UMSE)	1298.2		1596.4		1168.6		470.5	
Systematic MSE (SMSE)	632.9		504.4		30.2		11.5	
UMSE/MSE (%)	67.2		76.0		97.5		97.6	
SMSE/MSE (%)	32.7		24.0		2.5		2.4	

follows:

$$u(x) \simeq \sum_{i=1}^{N} u_i \phi_i(x), \tag{8}$$

where $u_i(x)$ is the coefficient for ith basis function. The error in satisfying the differential Eq. (7) with the N terms of the sum of Eq. (8) is

$$e_N = L\left(\sum_{i=1}^{N} u_i \phi_i\right) - f(x). \tag{9}$$

The Galerkin procedure requires that the error be orthogonal to each basis function in the following sense:

$$\int_a^b e_N \phi_j \, \mathrm{d}x = 0. \quad j = 1, 2, \ldots, N. \tag{10}$$

By substituting Eq. (9) into Eq. (10) the final form is obtained

$$\int_a^b \phi_j L\left(\sum_{i=1}^{N} u_i \phi_i\right) \mathrm{d}x - \int_a^b \phi_j f(x) \, \mathrm{d}x = 0. \tag{11}$$

This reduces the problem to N algebraic equations that relate the unknown coefficients u_i to the transforms of the forcing function.

If we chose the basis functions as tent-shaped, piecewise linear functions, which are also called chapeau functions as shown in Fig. 9, the basis functions decrease linearly to zero at $x = (i-1)\Delta x_{i-1}$, and $(i+1)\Delta x_{i+1}$, and it is zero everywhere else. Mathematically $\phi_i(x)$ is defined as follows:

$$\phi_i(x) = \begin{cases} 0, & x > (i+1)\Delta x_{i+1} \text{ or } x < (i-1)\Delta x_{i-1}, \\ [x - (i-1)\Delta x_{i-1}]/\Delta x_i, & (i-1)\Delta x_{i-1} \leqslant x \leqslant i\Delta x_i, \\ [(i+1)\Delta x_{i+1} - x]/\Delta x_{i+1}, & i\Delta x_i \leqslant x \leqslant (i+1)\Delta x_{i+1}. \end{cases} \tag{12}$$

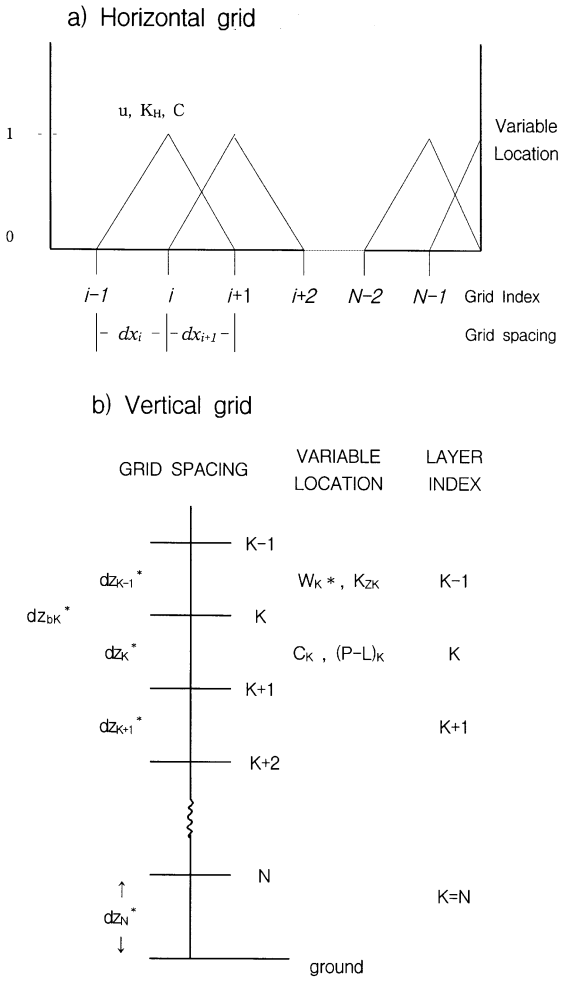

Fig. 9. (a) The horizontal grid as well as the chapeau basis functions and (b) the vertical grid with non-uniform spacing, dz^*.

Note that the coefficient u_i is actually the value of the function at $x = i\Delta x_i$ since $\phi_i(i\Delta x_i) = 1$ and $\phi_j(j\Delta x_j) = 0$ for $i \neq j$. If $f(x)$ in Eq. (11) is approximated in terms of the basis functions such that

$$f(x) = \sum_{i=1}^{N} f_i \phi_i \tag{13}$$

Eq. (11) becomes

$$\int_a^b \phi_j L\left(\sum_{i=1}^{N} u_i \phi_i\right) \mathrm{d}x - \sum_{i=1}^{N} f_i \int_{(j-1)\Delta x_{j-1}}^{(j+1)\Delta x_{j-1}} \phi_j \phi_j \, \mathrm{d}x = 0. \tag{14}$$

The evaluation of Eq. (14) yields to a finite element expansion form.

A.2. The numerical analogs of the tracer continuity equation

The finite form of the horizontal component of the tracer continuity equation is given by

$$A_i C_{i-1}^{t+1} + B_i C_i^{t+1} + D_i C_{i+1}^{t+1} = E_i C_{i-1}^{t} + F_i C_i^{t} + G_i C_{i+1}^{t}, \tag{15}$$

where C_i^t is the concentration at time step t and grid location i, while

$$A_i = \frac{\mathrm{d}x_i}{\tau} - \mu\alpha_i, \quad B_i = \frac{2}{\tau}(\mathrm{d}x_i + \mathrm{d}x_{i+1}) + \mu\beta_i,$$

$$D_i = \frac{\mathrm{d}x_{i+1}}{\tau} + \mu\gamma_i, \quad E_i = \frac{\mathrm{d}x_i}{\tau} + (1-\mu)\alpha_i,$$

$$F_i = \frac{2}{\tau}(\mathrm{d}x_i + \mathrm{d}x_{i+1}) - (1-\mu)\beta_i,$$

$$G_i = \frac{\mathrm{d}x_{i+1}}{\tau} - (1-\mu)\gamma_i.$$

where τ is the time step and μ is the Crank–Nicolson parameter whose value is $\frac{1}{2}$, and

$$\alpha_i = (\mu_i + 2u_{i-1}) + 3(K_i + K_{i-1})/\mathrm{d}x_i,$$

$$\beta_i = (-u_{i-1} + u_{i+1}) + 3[(K_{i-1} + k_i)\,\mathrm{d}x_{i+1} + (K_i + K_{i+1})\,\mathrm{d}x_i]/\mathrm{d}x_i\,\mathrm{d}x_{i+1},$$

$$\gamma_i = (u_i + 2u_{i+1}) - 3(K_i + K_{i+1})/\mathrm{d}x_{i+1}.$$

The vertical component of the tracer continuity equation is expressed in the finite form as

$$A_k C_{k+1}^{t+1} - B_k C_k^{t+1} - D_k C_{k-1}^{t+1} = -A_k C_{k+1}^{t} + E_k C_k^{t} + D_k C_{k-1}^{t} - F_k, \tag{16}$$

where

$$A_k = W_{k+1}^* + \frac{(K_{k+1} + K_k)}{\mathrm{d}z_{k+1}^*}\left(\frac{\bar{s}}{\bar{s} - z_g}\right),$$

$$B_k = 2\frac{(\mathrm{d}z_k^* + \mathrm{d}z_{k+1}^*)}{\tau}\left(\frac{\bar{s} - z_g}{\bar{s}}\right) + \left(\frac{\bar{s}}{\bar{s} - z_g}\right) \times \left(\frac{K_{k-1} + K_k}{\mathrm{d}z_k^*} + \frac{K_{k+1} + K_k}{\mathrm{d}z_{k+1}^*}\right),$$

$$D_k = W_{k-1}^* - \frac{K_{k-1} + K_K}{\mathrm{d}z_k^*}\left(\frac{\bar{s}}{\bar{s} - z_g}\right),$$

$$E_k = \left(\frac{\bar{s}}{\bar{s} - z_g}\right)\left(\frac{K_{k-1} + K_k}{\mathrm{d}z_k^*} + \frac{K_{k+1} + K_k}{\mathrm{d}z_{k_1^*}}\right) - 2\frac{(\mathrm{d}z_k^{*+}\mathrm{d}z_{k+1}^*)}{\tau}\left(\frac{\bar{s} - z_g}{\bar{s}}\right),$$

$$F_k = 2(P - L)_k\,(\mathrm{d}z_k^* + \mathrm{d}z_{k+1}^*).$$

A.3. The boundary flux

Expanding the Galerkin integral of the advection term by parts yields the first boundary flux as $(u_1 + K_1/\mathrm{d}x_2)(C_1^t + C_1^{t+1})$. From Eq. (15), the required integration results in

$$A_1 = 0, \quad E_1 = 0,$$

$$B_1 = \frac{2\mathrm{d}x_2}{\tau} + \mu\beta, \quad D_1 = \frac{\mathrm{d}x_2}{\tau} + \mu\gamma,$$

$$F_1 = \frac{2\mathrm{d}x_2}{\tau} - (1-\mu)\beta, \quad G_1 = \frac{\mathrm{d}x_2}{\tau} - (1-\mu)\gamma \tag{17}$$

with

$$\beta = -4u_1 + u_2 + \frac{3(K_1 + K_2)}{\mathrm{d}x_2},$$

$$\gamma = u_1 + 2u_2 - \frac{3(K_1 + K_2)}{\mathrm{d}x_2}.$$

For the Nth boundary

$$A_N = \frac{\mathrm{d}x_N}{\tau} - \mu\alpha, \quad B_N = 2\frac{\mathrm{d}x_N}{\tau} + \mu\beta, \quad D_N = 0,$$

$$E_N = \frac{\mathrm{d}x_N}{\tau} + (1-\mu)\alpha,$$

$$F_N = \frac{2\mathrm{d}x_N}{\tau} - (1-\mu)\beta, \quad G_N = 0 \tag{18}$$

with

$$\alpha = u_N + 2u_{N-1} + \frac{3(K_N + K_{N-1})}{\mathrm{d}x_N},$$

$$\beta = 4u_N - u_{N-1} + \frac{3(K_N + K_{N-1})}{\mathrm{d}x_N}.$$

These boundary conditions provide that the concentration will flow smoothly off or onto the grid with the flow as $(u_1 + K_1/\mathrm{d}x_2)(C_1^t + C_1^{t+1})$ in the first boundary and $(u_N + K_N/\mathrm{d}x_N)(C_N^t + C_N^{t+1})$ in the Nth boundary.

Appendix B

In the surface layer, the vertical diffusivity is computed according to Monin–Obukhov similarity theory

$$K_z = \frac{kzu_*}{\Phi_k(z/L)}, \tag{19}$$

where k is the von-Karmann constant, L the Monin–Obukhov length scale, u_* the friction velocity and $\Phi_k(z/L)$ the non-dimensional concentration profile function which is the function of stability L. The nondimensional concentration profile function $\Phi_k(z/L)$ is assumed to be similar to that of heat. According to Businger et al. (1971) $\Phi_k(z/L)$ is given by

$$\Phi_k = 0.74 + 4.7\frac{z}{L} \quad \text{for } \frac{z}{L} > 0,$$

$$\Phi_k = 0.74 \quad \text{for } \frac{z}{L} = 0, \tag{20}$$

$$\Phi_k = 0.74\left(1 - 9\frac{z}{L}\right)^{-1/2} \quad \text{for } \frac{z}{L} < 0.$$

Above the surface layer, but within the planetary boundary layer during stable or neutral condition ($z/L \geqslant 0$), the surface layer formulation is extended by an empirical function of height based on the results of second-order closure modeling by Brost and Wyngaard (1978),

$$K_z = \frac{kzu_*(1 - z/z_i)^{3/2}}{\Phi_k(z/L)}, \tag{21}$$

where z_i is the height of the planetary boundary layer.

In the convective boundary layer above the surface layer

$$K_z = kw_*z\left(1 - \frac{z}{z_i}\right), \tag{22}$$

where w^* is the convective velocity.

In the stable boundary layer, z_i is determined by

$$z_i = \min\left(k\left[\frac{u_*L}{f}\right]^{1/2}, \quad 0.3\frac{u_*}{f}\right), \tag{23}$$

where f is the Coriolis parameter.

Above the planetary boundary layer, the eddy diffusion coefficient is determined as a function of local Richardson number and vertical wind shear derived by Blackadar (1976) from second-order closure theory

$$K_z = K_0 + S(k-l)^2\frac{R_c - R_i}{R_c} \tag{24}$$

where $K_0 = 1.0\,\mathrm{m^2\,s^{-1}}$, $l = 100\,\mathrm{m}$, R_c the critical Richardson number is 0.25, S is vertical wind shear, $R_i = g/\bar{\theta}S^2\,\mathrm{d}\theta/\mathrm{d}z$ where θ is the potential temperature and g the gravity. When the Richardson number exceeds the critical value, then set $K_z = K_0$.

References

Blackadar, A.K., 1976. Modeling nocturnal boundary layer. Proceedings of 3rd Symposium on Atmospheric Turbulence. American Meteorological Society, pp. 46–49.

Brost, R.A., Wyngaard, J.C., 1978. A model study of the stably stratified planetary boundary layer. Journal of Atmospheric Science 35, 1427–1440.

Businger, J.A., Wyngaard, J.C., Izumi, Y., Bradley, E.F., 1971. Flux profile relationships in the atmospheric surface layer. Journal of Atmospheric Science 28, 181–189.

Carmichael, G.R., Kitada, T., Peters, L.I., 1980. Application of a Galerkin finite element method to atmospheric transport problems. Computers and Fluids 8, 155–176.

Carmichael, G.R., Peters, L.K., Kitada, T., 1986. A second generation model for regional-scale transport/chemistry/deposition. Atmospheric Environment 20, 173–188.

Chock, D.P., Dunker, A.M., 1983. A comparison of numerical methods for solving the advection equation. Atmospheric Environment 17, 11–24.

Davis, C.G., Bunker, S.S., Mutschlecner, J.P., 1984. Atmospheric transport models for complex terrain. Journal of Applied Meteorology 23, 234–238.

Fast, J.D., O'Steen, B.L., Addis, R.P., 1995. Advanced atmospheric modeling for emergency response. Journal of Applied Meteorology 34, 626–649.

Fox, D.G., 1981. Judging air quality model performance. Bulletin of American Meteorological Society 62, 599–609.

Haltiner, G.J., Williams, R.T., 1980. Numerical Prediction Dynamic Meteorology. Wiley, New York, 379pp.

Jung, Y.-S., Park, S.-U., Yoon, I.-H., 1996. Characteristic features of local air quality associated with meteorological conditions. Journal of Korean Meteorological Society 32(2), 271–290 (in Korean).

Lange, R., 1978. ADPIC — a three-dimensional particle-in-cell model for the dispersion of atmospheric pollutants and its comparison with regional tracer studies. Journal of Applied Meteorology 17, 320–329.

Mahlman, D.J., Sinclair, R.W., 1977. In: Suffet, I. H. (Ed.), Part 1. Fate of Pollutants in the Air and Water Environments. Wiley, New York, pp. 223–252.

Mahrer, Y., Pielke, R.A., 1977. A numerical study of the airflow over irregular terrain. Beitr Phys. Atmos. 50, 96–113.

National Institute of Environmental Research, 1994. Study on visibility and smog phenomena in Seoul Metropolitan area. NIER Report No. 94-27-442, 158pp.

Park, S.-U., 1992. Estimation of the wind profile in the boundary layer using routine meteorological data. Journal of Korean Meteorological Society 28, 417–433.

Park, S.-U., 1994. Air quality simulations using surface meteorological observation data. Journal of Korean Meteorological Society 30(3), 469–486.

Pepper, D.W., Kern, C.D., Long, P.E. Jr., 1979. Modeling the dispersion of atmospheric pollution using cubic splines and chapeau functions. Atmospheric Environment 13, 223–237.

Pielke, R.A., 1984. Mesoscale Meteorological Modeling. Academic Press, New York, 612pp.

Pielke, R.A., Cotton, W.R., Walko, R.L., Tremback, C.J., Lyons, W.A., Grasso, L.D., Nicholls, M.E., Moran, M.D., Wesley, D.A., Copeland, J.H., 1992. A comprehensive meteorological modeling system – RAMS. Meteorology and Atmospheric Phys. 49, 69–91.

Rao, S.T., Sistla, G., Pagnotti, V., Peterson, W.B., Irwin, J.S., Tunner, D.B., 1985. Evaluation of the performance of Ram with the regional air pollution study data base. Atmospheric Environment 19, 1503–1518.

Scherman, C.A., 1978. A mass consistent model for wind field over complex terrain. Journal of Applied Meterology 17, 312–319.

Toon, O.B., Turco, R.P., Westphal, D., Malone, R., Liu, M.S., 1988. A multidimensional model for aerosols: description of computational analogs. Journal of Atmospheric Science 45, 2123–2143.

Touma, J.S., Irwin, J.S., Tikvart, J.A., Coulter, C.T., 1995. A review of procedures for updating air quality modeling techniques for regulatory programs. Journal of Applied Meteorology 34, 731–737.